Mapping Snow Grain Size over Greenland from MODIS

Alexei Lyapustin[a,b], Marco Tedesco[b,c,e], Yujie Wang[a,b], Alexander Kokhanovsky[d]

[a]GEST center, University of Maryland, Baltimore county, Catonsville, MD 21228, USA

[b]NASA Goddard Space Flight Center, Mail code 614.4, Greenbelt, MD 20771, USA

[c]City College of New York - CUNY, 138 and Convent Ave., New York, NY 10031, USA

[d]Institute of Environmental Physics, University of Bremen, O. Hahn Allee 1, D-28334 Bremen, Germany

[e]JCET center, University of Maryland, Baltimore County, MD, 21228, USA

Abstract.

This paper presents a new automatic algorithm to derive optical snow grain size (SGS) at 1 km resolution using Moderate Resolution Imaging Spectroradiometer (MODIS) measurements. Differently from previous approaches, snow grains are not assumed to be spherical but a fractal approach is used to account for their irregular shape. The retrieval is conceptually based on an analytical asymptotic radiative transfer model which predicts spectral bidirectional snow reflectance as a function of the grain size and ice absorption. The analytical form of solution leads to an explicit and fast retrieval algorithm. The time series analysis of derived SGS shows a good sensitivity to snow metamorphism, including melting and snow precipitation events. Pre-processing is performed by a Multi-Angle Implementation of Atmospheric Correction (*MAIAC*) algorithm, which includes gridding MODIS data to 1 km resolution, water vapor retrieval, cloud masking and an atmospheric correction. *MAIAC* cloud mask (CM) is a new algorithm based on a time series of gridded MODIS measurements and an image-based rather than pixel-based processing. Extensive processing of MODIS TERRA data over Greenland shows a robust performance of CM algorithm in discrimination of clouds over bright snow and ice. As part of

the validation analysis, SGS derived from MODIS over selected sites in 2004 was compared to the microwave brightness temperature measurements of SSM\I radiometer, which is sensitive to the amount of liquid water in the snowpack. The comparison showed a good qualitative agreement, with both datasets detecting two main periods of snowmelt. Additionally, MODIS SGS was compared with predictions of the snow model CROCUS driven by measurements of the automatic whether stations of the Greenland Climate Network. We found that CROCUS grain size is on average a factor of two larger than MODIS-derived SGS. Overall, the agreement between CROCUS and MODIS results was satisfactory, in particular before and during the first melting period in mid-June. Following detailed time series analysis of SGS for four permanent sites, the paper presents SGS maps over the Greenland ice sheet for the March-September period of 2004.

1. Introduction

Snow grain is arguably the most fascinating parameter within a snowpack, because of the different geometries that ice grains can exhibit: from large cup shaped grains of depth hoar, to stellar flakes characterizing new snow, and big structures of grape-shaped rounded crystals of melted/refrozen snow. First observations of snowflakes were reported by Kepler (1611) and Descartes (Frank, 1974), the former pondering the question on why the snow crystals exhibit a six-fold symmetry and the latter being the first to provide a morphological description of snow crystals. Later on, in 1665 Robert Hooke (2003) published a volume containing sketches of objects observed with the microscope, including snow crystals. More recently, Wilson A. Bentley (1931) in 1931 performed microphotography of a large number of snow crystals and Ukichiro Nakaya (1954) in 1954 performed the first systematic study of snow crystals. The

current methods of studying the shape and size of ice crystals can be found in review by Domine et al. (2008).

Grain size is a fundamental parameter for characterizing snowpack properties: for example, the thermodynamic state of a snowpack is related to grain size because of the metamorphism determined by gradients of temperature and vapor; specific snow area and snow diffusivity, which are primary factors in snow chemistry of gases, are related to the snow grain size; spectral snow albedo, playing a key role in the Earth's radiation balance, is largely controlled by the grain size (e.g., Domine et al., 2008).

Space-borne remote sensing of the Earth in the visible and shortwave infra-red (SWIR) regions has been used for estimating grain size at large spatial scales and moderate-to-high spatial resolution. In the past 10-15 years there has been a substantial body of research on retrieval of the snow grain size and absorptive impurities by soot or dust from satellite observations. A comprehensive overview of these works has recently been given by Stamnes et al. (2007). The proposed methods commonly rely on the fact that the absorption of pure ice is very low in the visible, but grows to moderate/strong in the NIR/SWIR (Wiscombe and Warren, 1980). Because ice is highly transparent in the visible, its reflectance has a weak dependence on the grain size and a high sensitivity to absorption by impurities. In the NIR region, the ice absorption increases, and snow reflectance becomes strongly dependent on the grain size as well as amount of soot. Finally in the SWIR, the ice absorption becomes dominant, and snow reflectance depends mainly on the grain diameter.

The retrieval of snow grain size (SGS) relies on the model of snow reflectance as a function of snow properties, viewing geometry and wavelength. Commonly, Mie theory (Mie, 1908) has been used for this purpose, and different studies relied on the assumption of spherical particles

for SGS retrievals (e.g., Nolin & Dozier, 1993; Painter et al., 2003; Stamnes et al., 2007). In the past decade, an analytical asymptotic radiative transfer (AART) snow model was developed which accounts for irregular shapes of snow grains (Kokhanovsky & Zege, 2004; Kokhanovsky et al., 2005; Kokhanovsky, 2006). Recently, Tedesco and Kokhanovsky (2007) applied AART with the Koch model of fractal particles for retrieving SGS from the near-infrared measurements of the Moderate Resolution Imaging Spectroradiometer (MODIS). The analysis of that paper also identified a high sensitivity of the retrieved grain size to the errors of atmospheric correction. The largest impact, in particular in operational applications, is produced by errors in cloud detection over snow.

In this study, we apply a new Multi-Angle Implementation of Atmospheric Correction (*MAIAC*) algorithm (Lyapustin and Wang, 2007) and AART snow model for the SGS retrieval over the Greenland ice sheet (GIS) using data collected by the MODIS instrument flying onboard the TERRA satellite. An improved knowledge of the temporal evolution of grain size at large spatial scales over Greenland is useful for refining surface melting detection techniques from other satellite data sets (e.g., Tedesco, 2007a) and for understanding how processes such as increased melting (e.g., Tedesco, 2007b) affect the surface energy balance and vertical stratigraphy and precipitation events (in both timing and extent) over the GIS. Because of the paucity of grain size measurements over the GIS and of the dependency of these measurements on the operator's ability and skills, results derived from MODIS data are compared with those obtained with a snow model driven with surface meteorological data recorded on ground by the Greenland Climate Network (GC-Net) automatic stations.

The paper is structured as follows: in Section 2 we discuss *MAIAC* cloud detection and atmospheric correction, and provide detail of the AART snow model. The algorithm of SGS

retrieval is described in section 3. In Section 4 we focus on the results obtained for selected sites over the GIS, and on the comparison between satellite-derived SGS and those obtained with a snow model. A qualitative analysis between MODIS SGS and microwave data measured by the Special Sensor Microwave Imaging (SSM/I) radiometer is also reported. We discuss the results in section 5 and dedicate the last Section to the summary.

2. Method Description

MAIAC is a new algorithm which uses a time series of MODIS measurements and combines image- and pixel-level processing to detect clouds and perform simultaneous retrievals of aerosol properties and surface bidirectional reflectance and albedo (Lyapustin and Wang, 2007). The algorithm is generic although the aerosol retrievals are currently not performed over snow. In this work, we are using a reduced *MAIAC* processing, which includes cloud mask, water vapor retrievals and a simplified form of atmospheric correction described in sections 2.1-2.2.

2.1 Cloud Mask Algorithm

The central idea of *MAIAC* cloud mask (CM) algorithm is to build and dynamically update a reference clear-skies image of the surface (*refcm*), which is further used as a comparison target for cloud detection. With a high frequency of global MODIS observations, the land surface can be considered as a static or slowly changing background contrary to ephemeral clouds. In cloud-free conditions, the consecutive images of the same surface area have a well-reproducible spatial pattern and a high spatial correlation. Clouds introduce distortions in this pattern usually in a random way reducing the correlation, which can be detected by covariance analysis. The

covariance is a metric showing how well the two images X and Y correlate over an area of $N \times N$ pixels,

$$\mathrm{cov} = \frac{1}{N^2}\sum_{i,j=1}^{N}\frac{(x_{ij}-\bar{x})(y_{ij}-\bar{y})}{\sigma_x\sigma_y},\ \sigma_x^2 = \frac{1}{N^2}\sum_{i,j=1}^{N}(x_{ij}-\bar{x})^2\ . \quad (1)$$

Because covariance removes the average component of the signals, this metric is equally successful over the dark and bright surfaces and in both clear and hazy conditions if the surface spatial variability is still detectable from space.

The *MAIAC* algorithm starts with accumulation of 6-16 days of MODIS data in the processing Queue. The size of the Queue depends on the frequency of MODIS observations over a given location, which is defined by the latitude. *MAIAC* uses 16 days for the Earth equator where MODIS makes one observation per day, and 6 days for the poles, which feature several orbits per day. For the time series analysis, MODIS data are gridded to 1 km resolution, creating *Tiles* of data.

The covariance analysis is applied for the areas of 25×25 km^2, called blocks, using band 1 (0.645 μm) data. When the cloud-free conditions for a given block are found, the image is copied to the reference image (*refcm*), which is further used to compute covariance with the new MODIS measurements. Each time the new measurements are identified as cloud-free for a given block, the *refcm* is updated thus dynamically adapting to seasonal variations of the landcover. In order to account for the effects related to scan angle variation, e.g. pixel size growth, surface BRF effect or reduction of contrast at higher view zenith angles (VZA), two reference clear-skies images are maintained by the algorithm, *refcm1* for the view zenith angle range VZA≈0-45^o and *refcm2* for VZA=45^o-60^o. In addition to *refcm*, the maximal value ($r1_{max}$) and the variance (σ_1) of reflectance in band 1 as well as the brightness temperature contrast ($\Delta BT = BT_{max} - BT_{min}$) for each

surface block are also stored in the memory. Analysis of MODIS data shows that thermal contrast (ΔBT) is a rather stable metric of a given land area in clear conditions. In partially cloudy conditions, the contrast increases because BT_{min} is usually lower over clouds.

The new CM algorithm has an internal surface classifier, producing a dynamic land-water-snow (*LWS*) mask, and a surface change mask. These are an integral part of *MAIAC* guiding the cloud masking when the surface changes rapidly as a result of fires, floods or snow fall/ablation.

The final values of the *MAIAC* cloud mask are clear (CM_CLEAR, CM_CLEAR_WATER, CM_CLEAR_SNOW), indicating surface type as well, possibly cloudy (CM_PCLOUD), and confidently cloudy (CM_CLOUD). The covariance component of *MAIAC* algorithm, which offers a direct way to identify clear conditions, renders another commonly used value of cloud mask – "possibly clear" – redundant. The full description of the algorithm, including the logic of cloud detection at a pixel level, is given in (Lyapustin et al., 2008).

The current version of CM algorithm was developed for generic land applications. It may need further enhancements for Arctic applications, such as discrimination of the sea ice. Nevertheless, we found that it has a good performance over the snow detecting significantly more clear snow pixels than the operational MODIS cloud mask algorithm MOD35 (Lyapustin et al., 2008).

An example of *MAIAC* cloud mask for Thule located on the north-west of Greenland (77º30'0N, 69º10'0W), is shown in Figure 1. The image shows 6 consecutive daytime MODIS TERRA gridded images for two days 112-113, 2004, for the area of 150×150 km^2. The two left columns show the TERRA RGB images. They are differently normalized to help distinguish clouds from the bright snow. The central feature in the image shows a fiord covered by snow/ice, which melts in the summer.

The right column shows the derived cloud mask, which uses the following legend: red – cloud; white, blue and light blue – clear over snow, land and water, respectively. A reproducible spatial pattern helps to identify cloud-free blocks of the surface. The top three images represent the clear-skies conditions. The second image is obtained near the edge of scan and has an apparently coarser resolution than images 1 and 3, acquired close to nadir. Clouds are seen in the images 4-6 as distortions to the spatial pattern of reflectance. For the most part, they are captured by the cloud mask algorithm.

2.2 Atmospheric Correction of MODIS Data

The aerosol concentration over Greenland is generally low (Tomasi et al., 2007), except events of transported biomass burning smoke or pollutions from Northern America or Eurasia. Because of high surface reflectivity and cloud contamination, reliable remote sensing methods for aerosol retrievals over this region of the world do not exist. For these reasons, we only consider effects of Rayleigh scattering and molecular absorption, including that of water vapor and ozone.

Table 1 shows the effective center wavelengths of MODIS TERRA 500 m bands, the in-band optical thickness of absorption by well-mixed gases, and of water vapor absorption at the column amount of 1 cm. The effective band center wavelength is defined as a wavelength for which monochromatic and narrow-band direct vertical transmittances of the aerosol-free atmosphere are equal:

$$\exp\{-\tau^R(\lambda_C)\} = \int_{\Delta\lambda} F_\lambda \exp\{-\tau^R(\lambda)\} h_\lambda d\lambda \Big/ \int_{\Delta\lambda} F_\lambda h_\lambda d\lambda \,, \qquad (2)$$

where F_λ is extraterrestrial spectral solar irradiance, h_λ is relative spectral response (RSR) function of MODIS TERRA bands, and τ^R is Rayleigh optical thickness computed with model of

Bodhaine et al. (1999). The optical thickness of the in-band gaseous or water vapor absorption is defined similarly. The optical thickness of absorbing gases is calculated for the carbon dioxide concentration of 380 *ppm*, and concentration of other gases corresponding to the Arctic atmospheric model (Kneizys et al., 1996). The calculations included absorption of 6 major atmospheric gases (H_2O, CO_2, CH_4, NO_2, CO, N_2O) with line parameters from HITRAN-2000 (Rothman et al., 2003) database using the Voigt vertical profile, and the Atmospheric Environmental Research continuum absorption model (Mlawer et al., 2006).

The top-of-atmosphere (TOA) reflectance is modeled in this work using a modified Lambertian formulation, and assuming that most of the ozone absorption takes place above the molecular atmosphere:

$$R_{\Delta\lambda}(\mu_0,\mu,\varphi) \cong (R^A_{\Delta\lambda}(\mu_0,\mu,\varphi) + \frac{\rho(\mu_0,\mu,\varphi)T_{\Delta\lambda}(\mu_0,\mu)}{1-q(\mu_0)s_{\Delta\lambda}})T^{Ozone}_{\Delta\lambda}(\mu_0,\mu) \quad (3)$$

where R^A is atmospheric path reflectance, T is the total upward and downward atmospheric transmittance, s is spherical albedo of the atmosphere, ρ and q are the surface bidirectional reflectance factor (BRF) and albedo, respectively. The subscript indicates that the functions are weighted with respective RSR of MODIS channels:

$$R_{\Delta\lambda} = \int F_\lambda R_\lambda h_\lambda d\lambda \Big/ \int F_\lambda h_\lambda d\lambda \,. \quad (4)$$

Because atmospheric optical thickness over Greenland is low, correction using Lambertian equation (3) is rather accurate even at relatively low sun zenith angle (Lyapustin, 1999). The atmospheric correction is based on the look-up table computed using radiative transfer code SHARM (Lyapustin, 2005) and the Interpolation and Profile Correction (IPC) method (Lyapustin, 2003) for narrow-band and shortwave broadband calculations.

After generating cloud mask, *MAIAC* retrieves column water vapor with a relative accuracy of 5-10% from MODIS NIR channels 17-19 located in the water vapor absorption band 0.94 μm using a band ratio technique (Lyapustin and Wang, 2007). The retrieved values over Greenland for the period covering spring to fall of 2004 agree well with known climatology showing the average values of 0.2-0.4 cm for the spring and autumn, and 0.4-0.8 cm for the summer period (Kneizys et al., 1996).

Because of significant surface height variation over Greenland, the height/pressure correction is implemented for functions R^A, T and s in the visible and near infrared bands 1-4 as described in (Lyapustin and Wang, 2007).

2.3 Snow Reflectance Model

In this work, we are using the AART model of snow reflectance developed by Kokhanovsky and Zege (2004). This model predicts snow reflectance using an asymptotic analytical solution of the radiative transfer problem in semi-infinite media with low absorption (the so-called Milne problem), which is a good approximation for snow in the visible spectral range:

$$\rho = R_0(\mu_0, \mu, \varphi)\exp(-A(\mu_0, \mu, \varphi)\sqrt{\gamma d}\,). \quad (5)$$

Here, $\gamma = 4\pi\chi/\lambda$, χ is imaginary part of refractive index of ice, λ is the wavelength, and $d=6\langle V\rangle/\langle S\rangle$ is the effective grain size defined by the ratio of the average volume to the average surface area of grains. R_0 is a solution of radiative transfer equation for snow with zero absorption. For simplicity, we assume that R_0 does not depend on snow grain size because the wavelengths at consideration (0.4–2.1 μm) are much smaller than parameter d, which is known

to vary from about 50 μm for fresh snow to 1-1.5 mm in pre-melting conditions (Wiscombe and Warren, 1980) to several millimeters during snowmelt. The function A relates to the photon's escape probability from the media. For the fractal ice particles, it can be approximated as follows:

$$A(\mu_0, \mu, \varphi) \cong 0.66(1+2\mu_0)(1+2\mu) / R_0(\mu_0, \mu, \varphi)\,. \quad (6)$$

Comparison of the described analytical model with the accurate radiative transfer solution showed the accuracy of better than about 3% for zenith angles below ≈78°. A local validation of the model in the spectral range of 0.535-2.21 μm with field measurements has also demonstrated a good angular and spectral agreement (Kokhanovsky et al, 2005).

The described snow reflectance model has several limitations. First, as we mentioned, the zenith angles cannot be too high, which may limit retrievals over polar regions on winter, early spring and late fall when solar zenith angle is low. Second, comparisons with measurements showed that the model is not applicable near the forward scattering (glint) direction ($\varphi \sim 0^0$). Third, the model was derived with the assumption of low absorption, $\beta = \sqrt{\gamma d} << 1$. This assumption holds well for MODIS vis-NIR bands 1-5, but in the shortwave infrared region for bands 6 (1.6 μm) and 7 (2.1 μm) parameter β may be as high as 0.5-1 during snowmelt. On the other hand, ground-based measurements of the bidirectional reflectance of snow (Kokhanovsky et al, 2005) and processing of AATSR data (Kokhanovsky and Schreirer, 2007) showed that the model can be used in the SWIR region as well.

In general, the snow model should include the absorption of light by liquid water in snow (Green et al., 2002), and also by absorbing impurities, such as soot from biomass burning and urban-industrial aerosols (Warren, 2007), or transported dust. In this work, however, we did not find

the evidence from MODIS data of measurable soot contamination over the Greenland in 2004, at least above sensitivity of our model. Our analysis also showed that adding water absorption has almost no effect in the MODIS bands used for the grain size retrievals because the imaginary part of the refractive index is nearly the same. For these reasons, we decided not to consider these sources of absorption further.

An obvious advantage offered by this model is an explicit dependence on the grain size and snow refractive index. This model offers a straightforward and very effective inversion scheme, which would only require tabulating function R_0 as a function of angles. For this work, the LUT of function R_0 was computed with the radiative transfer code SHARM (Lyapustin, 2005) using the scattering function for random fractal crystals (Mischenko et al., 1999). Mischenko provides 2000 Legendre expansion coefficients. We found that SHARM solution achieved convergence with an accuracy of about 0.1-0.2% when we used 1024 coefficients.

The last row of Table 1 shows the band-average imaginary part of an effective refractive index of ice $\overline{\chi}_e^{ice}$, based on the latest compilation of Warren and Brandt (2008), which is computed from equation

$$\exp(-A(\mu_0,\mu,\varphi)\sqrt{\frac{4\pi\overline{\chi}_e^{ice}d}{\lambda_C}}) = \int \exp(-A(\mu_0,\mu,\varphi)\sqrt{\frac{4\pi\chi^{ice}(\lambda)d}{\lambda}})F_\lambda h_\lambda d\lambda \Big/ \int F_\lambda h_\lambda d\lambda \,. \qquad (7)$$

The effective value accounts for spectral variations of $\chi^{ice}(\lambda)$ within the band-pass interval, for variations of function A≅0.4-2.2 with the MODIS viewing geometry, and for changes of diameter during snowmelt. We found that using effective values improves spectral agreement between the model and the MODIS measurements in the NIR and SWIR bands.

3. Method of Grain Size Retrievals

The developed algorithm has several processing stages: *a*) gridding MODIS level 1B geolocated and calibrated data to 1 km resolution; *b*) retrieving water vapor; *c*) cloud masking; *d*) performing atmospheric correction; *e*) retrieving snow properties.

The snow grain size can be derived from satellite data using either a single channel (e.g. Nolin and Dozier, 1993; Stamnes et al., 2007), or often used band-ratio algorithms (e.g., Scambos et al., 2007). The first approach requires an accurate knowledge of the bidirectional reflectance R_0. We analyzed the accuracy of the modeled function R_0 experimentally by comparing it with the atmospherically corrected MODIS TERRA reflectance for a full range of viewing geometries and conditions during 7 months (March – September) of 2004 over Greenland. Figure 2 shows a comparison for the Blue (B3) band for the cloud-free observations, as detected by *MAIAC* cloud mask for the Saddle site (66.0006N, 44.5014W). Figure 2a shows the results for all view angles with geometry plotted in the bottom Figure 2c. The spikes of the function R_0 correspond to the glint directions where the AART model is not valid. It is interesting that MODIS measurements do not show significant increase of reflectance in the forward scattering directions. This result is typical not only for this particular site, but for the full area of Greenland. Figure 2b shows a reduced set of measurements where azimuthal angles $\varphi \leq 40^{o}$ were filtered. Although the agreement in this case is significantly better, the MODIS reflectance still shows less anisotropy than theoretical predictions. The main reason for this disagreement is a macroscopic surface roughness caused by the local terrain variations (slope and height variations), sastrugis, etc. There is a significant amount of such variability inside 1 km grid cell which flattens the BRF pattern of reflectance, and which is not taken into account by the plane-parallel radiative transfer model used to compute R_0 (e.g., Hudson et al., 2006; Hudson and Warren, 2007).

For this reason, we selected the band-ratio algorithm where the role of function R_0 is reduced to the second-order effect manifested through function A. Using two channels with different ice absorption, it is easy to obtain from Eq. (5):

$$d = \frac{1}{4\pi A^2}\left[\ln\left(\frac{\rho_1}{\rho_2}\right)\Big/\left(\sqrt{\chi_2/\lambda_2} - \sqrt{\chi_1/\lambda_1}\right)\right]^2 . \quad (8)$$

Because of R_0, there is some uncertainty in the magnitude of function A in equation (8), which may introduce some bias in the value of SGS. This function, however, depends only on the viewing geometry, so the possible bias should not affect the spatial variations of derived SGS. The calibration of the retrieved snow grain size with ground-based measurements can be used to improve the model of function A. Some preliminary results on such experimental calibration have been reported by Kokhanovsky (2006).

The example of retrieved snow grain size using the ratio $R_{1.24}/R_{0.65}$ is shown in the last column of Figure 1. Gridding allows an easy comparison between successive observations of the same area. The spatial pattern of the snow grain size is reproduced consistently for different observations on a single day and on successive days. The residual dependence on the VZA and on azimuth is small. In the retrievals, the forward scattering directions $\varphi \le 40^o$ were excluded.

A time series of retrieved grain size for the Saddle site is shown in Figure 3. Here, we used several different ratios created from bands 1 (0.645 μm), 2 (0.87 μm), and 5 (1.24 μm). The ratios R_5/R_1 and R_5/R_2 produce essentially the same results, showing very stable retrievals when no melting occurs, and a similar growth of SGS during the two periods of snowmelt. Another ratio R_2/R_1 (red line) used by Scambos et al., (2007) has a good sensitivity during snowmelt periods, but produces unstable results for the other periods with values often below 50 μm. Our

results suggest that the difference in the ice absorption between the Red and NIR bands may be too low for the reliable SGS retrievals when the grain size is small and no melting takes place.

The blue line shows SGS retrieved using Eq. (5) from a single band 6 (1.64 μm) where the ice absorption is high. A similar approach was used for SGS retrievals from the Global Imager (GLI) (Stamnes et al., 2007). In complete agreement with results from the above reference, this retrieval shows smaller values of SGS as compared to shorter wavelengths. The higher values of the retrieved grain size at shorter wavelengths are usually explained by a larger depth of penetration of light into the icepack (e.g. Li et al., 2001) and growth of the effective grain size with depth (Grenfell et al., 1994; Aoki et al., 2000).

Further, the ratio R_5/R_1 will be used as a baseline for our retrievals. In order to assess the sensitivity of the method we propose, the retrievals were conducted for different sites in the inland Greenland and compared with outputs of a snow energy balance model and the trends of space-borne microwave brightness temperature, which is described in the next section. Independently, we studied the behavior of SGS in the coastal regions of Greenland characterized by persisting melting and variations due to re-freeze and/or new snowfall. Figure 4 shows retrievals for the glacial area north-east of Thule shown by a red circle in the top-left image of Figure 4. There are several pronounced periods of systematic growth of the SGS, followed by a sharp drop. Some of these are selected by ovals in the figure. We have looked at periods 1 and 2 in detail trying to identify whether this is an uncertainty of the solution or it relates to a change of the state of snow. In both cases, the drop of SGS was preceded by a period of cloudiness, and it correlates with decrease of the measured SSM/I brightness temperature. The spatial RGB images are shown next to the time series of SGS. We cannot provide any detail for the first period (days 134-136) except clearing of the water from the sea ice. However, there was an evident fresh

snowfall during the extended 6-day period of cloudiness for the second period (days 211-217). On day 211 we see snow-free land along the melted water of the fiord. After 6 cloudy days, most of the bare land is covered by a new snow on day 217, with visible SGS decrease. This example shows that the developed method is sufficiently sensitive to detect snow metamorphism, associated with melting, re-freeze and fresh snowfall.

4. Comparisons with snow model outputs and microwave data

In this section, grain size values retrieved with MODIS are evaluated vs. those simulated with a snow physical model, CROCUS (Brun et al., 1989 and 1992). The need of comparing satellite-derived grain size with those obtained from a physical model is dictated by the lack of ground measurements, especially over the Greenland ice sheet. Even when they exist, these measurements are limited in space and time and therefore are limited in their usefulness for the evaluation of the algorithm proposed here.

Snow grain in CROCUS is defined in terms of optical size for albedo computation and physical size for stability assessment. The state of snow grains is also described through sphericity and dendricity (Brun et al., 1992). For the fresh snow, an initial value of 100 μm is set to the optical grain size while the initial values of dendricity and sphericity are obtained according to the surface wind. Then the snow metamorphoses and when the dendricity reaches 0 (from an initial value of -1), all the branched crystals have almost disappeared, and a size of 300 μm is applied. Grain size evolution is then computed according to the forcing data. In the following, forcing to the CROCUS model is derived from measurements of the automatic whether stations of the Greenland Climate Network (GC-Net, Steffen et al., 1996).

Beside the results from CROCUS, a qualitative analysis of the MODIS-retrieved grain size is also performed using data of the Special Sensor Microwave Imaging (SSM/I) radiometer. The microwave brightness temperature at 19.35 GHz, horizontal polarization, recorded by SSM/I is plotted for the cells containing the test site at resolution of 25 km. Microwave brightness temperature at 19.35 GHz is sensitive to the liquid water content within the snowpack (e.g., Tedesco et al., 2007). When snow melts, snow grains tend to bound to each others (constructive metamorphism) with the grain size of melted and/or refrozen snow generally greater than that of unthawed snow.

The comparison between MODIS-retrieved and CROCUS simulated SGS values, and brightness temperature was performed over four selected test sites: Dye-2 (66.4810N, 46.2800W), Saddle (66.0006N, 44.5014W), South Dome (63.1489N, 44.8167W) and NASA SE (66.4797N, 42.5002W). The results are shown in Figure 5. The MODIS results are averaged over an area of 25×25 km^2 for an easy comparison with SSM\I measurements. Note that CROCUS SGS is reduced by a factor of two. In this case, there is a good general agreement between CROCUS values and MODIS retrievals for the off-melting season and the first period of strong thawing (June, days 170-176). The best agreement for this period is observed for NASA SE and Saddle sites. For the Dye-2 and South-Dome sites, the maximum of melting is shifted by several days.

Overall, analysis of MODIS results suggest two well-expressed melting periods during the summer of 2004, with the second one occurring in August (days 220-226). One can see that CROCUS overestimates the length of melting period by almost 10 days over Saddle and South-Dome, but it fails to predict a strong melting event over site Dye-2. The SSM\I brightness temperature for this period of time supports the results obtained with MODIS.

Between June and August, CROCUS simulations predict additional intermediate high amplitude thawing periods for sites NASA-SE, Saddle and South-Dome, which are not detected with MODIS. Some of the disagreement between MODIS and CROCUS might be caused by cloudiness. Because of the inevitable errors in cloud detection, when cloudy pixels are masked as clear, the developed algorithm may produce lower SGS values in cloudy conditions. On the other hand, SSM\I data, which are not affected by cloudiness, do not support the predicted melting by CROCUS.

5. Seasonal melting over Greenland in 2004

Monitoring SGS over GIS can support the development of algorithms for snowmelt detection. The snow grain size retrieved from MODIS TERRA data for the melting period of 2004 over GIS is shown in Figure 6. Each image is obtained as a 3-day composite to cover gaps caused by clouds. Despite some inner areas remain un-initialized with our retrievals (shown by black color), the images provide a sufficiently good coverage and temporal resolution to detect short periods of melting.

The first image shows SGS for the middle of April, 2004. Note that we don't currently discriminate sea ice which has similar characteristics to snow of the inner regions of GIS. In May-June, melting takes place in the peripheral area of GIS and adjacent sea ice. The red color on the border of GIS indicates high SGS values. On the other hand, a relatively coarse resolution of our data (1 km) may result in undetected presence of pools of pure water cleared from sea ice along the shores, which will also be interpreted as higher SGS values.

Figures for the last week of June (days 169-175) show strong melting in the southern inner region of Greenland, as well as along the northern and western perimeter of GIS. The melting largely abates by day 178. In July, melting continues mainly in the north of Greenland. A second

period of melting begins in the middle of August. The strip of low values in the middle of southern GIS on day 223 is probably an artifact as this region was continuously covered by clouds.

We also studied the capabilities of our algorithm to produce spatially distributed SGS. A first step in this direction is to compare the maps of microwave brightness temperature with those of SGS. Figure 7 shows brightness temperature images of SSM\I for selected days of 2004. Low brightness temperature values are characteristics of dry snow whereas relatively high values are due to the presence of wet snow. From the visual comparison between microwave data and MODIS SGS, we observe that high brightness temperature values (melting snow) correspond to areas where grain size values are high. This is consistently true for all considered days.

6. Conclusions

Snow grain size is an important parameter, knowledge of which is required in various disciplines, from snow chemistry of gases to the Earth's radiation balance. The grain size, along with snow temperature and soot concentration, was an operational product of the Global Imager aboard Advanced Earth Observing Satellite-II (Hori et al., 2007) during its mission in 2003. In this paper, we described a new algorithm with operational capabilities to derive snow grain size from MODIS data over Greenland.

The new algorithm uses the framework of *MAIAC* processing to detect clouds, retrieve water vapor and perform atmospheric correction of MODIS measurements. Cloud discrimination over bright snow and ice surfaces is a very difficult problem, and robust performance of *MAIAC* CM algorithm is a key to successful retrieval of snow properties.

The SGS retrieval is based on the AART model, which predicts analytically the spectral and directional snow reflectance as an explicit function of snow grain size and absorption within the snowpack. We took advantage of the analytical form of solution to develop an explicit and fast SGS retrieval algorithm using the ratio of MODIS measurements in bands 5 (1.24 μm) and 1 (0.645 μm). Additional retrievals in the SWIR bands 6 (1.6 μm) and 7 (2.11 μm) with higher show absorption and lower light penetration depth can be used to evaluate the vertical profile of SGS (Li et al., 2001). The consistency of solution was demonstrated over the full range of the MODIS TERRA viewing geometries, excluding the forward scattering (glint) range of azimuthal angles ($\varphi \leq 40^{o}$), where the AART model is not valid. We also demonstrated the consistency of the time series of retrieved SGS and a good sensitivity of the algorithm to detect snowmelt and at least some of the snow precipitation events. The results of retrievals were compared for the year of 2004 with the microwave brightness temperature of SSM\I radiometer which is sensitive to amount of liquid water in the snow. The Greenland-scale comparisons show a good agreement in detection of two main melting periods in 2004, in the middle of June and in August. We believe that MODIS-based SGS retrievals may have a better sensitivity to the changes in snow metamorphism than the microwave measurements, in part due to significantly better spatial resolution (1 km vs 25 km), though temporal resolution might be affected by clouds presence.

MODIS retrievals were also compared with the snow model CROCUS driven with surface meteorological data recorded on ground by the Greenland Climate Network automatic stations for four different selected sites. Overall, the comparison was satisfactory, although the grain size of CROCUS is found to be on average a factor of two larger, and the number of predicted periods of thaw higher. There are certain differences in the magnitude and the longevity of the

main melting periods as well. The independent SSM\I results agree much better with MODIS retrievals than with CROCUS prediction results.

The performed comparison with SSM\I and CROCUS data, as well as good quantitative agreement with validated and published GLI results (Hori et al., 2007; Aoki et al., 2007) serve as an indirect validation of the described method. In the near future, we plan to extend validation to comparison with ground-based albedo measurements as well as available in situ grain size measurements.

The current algorithm is fast and can be run operationally. On the other hand, our processing model, although ensuring robust performance over Greenland, needs further development. We plan to include the light absorption by snow impurities, such as soot, in order to adapt the algorithm for the regions with high urban impact on snow. An enhancement is needed to discriminate sea ice based on MODIS data, and fine-tune *MAIAC* cloud mask for the Arctic environment. We demonstrated a sensitivity of method to detect fresh snowfall, but further work is needed to get to the point of automated classification of such events. One important part of research is developing a theoretical model to account for the surface roughness leading to reduced anisotropy of snow reflectance (function R_0) as compared to the currently used plane-parallel modeling approach. In this sense, MODIS is an excellent source of data with high frequency of observations over polar regions and a wide angular coverage.

Acknowledgement: The work of Dr. Lyapustin and Dr. Wang was supported by the NASA EOS Science (Dr. D. Wickland) and NPP (Dr. J. Gleason) grants.

Band N	B1	B2	B3	B4	B5	B6	B7
λ_C, μm	0.6449	0.8556	0.4655	0.5535	1.2419	1.6290	2.1131
τ^g	1.32e-3	1.82e-5	2.06e-3	4.60e-4	2.90e-3	1.01e-2	1.80e-2
τ^w, 1 *cm*	3.62e-3	5.49e-3	5.20e-5	3.63e-4	3.62e-3	0.87e-3	1.63e-2
$\overline{\chi}_e^{ice}$	1.25e-8	2.32e-7	1.05e-9	3.22e-9	1.20e-5	2.41e-4	(5.3÷6.8)e-4

Table 1. The center wavelength of MODIS TERRA land 500 m channels, the in-band absorption optical thickness of well-mixed gases and of 1 cm of water vapor, and effective refractive index of ice.

REFERENCES

Aoki, T., Aoki, Ta., Fukabori, M., Hachikubo, A., Tachibana, Y., & Nishio, F. (2000). Effects of snow physical parameters on spectral albedo and bidirectional reflectance of snow surface. *J. Geophys. Res.*, 105(D8), 10219−10236.

Aoki T, M. Hori, H. Motoyoshi, T. Tanikawa, A. Hachikubo, K. Sugiura, T. J. Y, R. Storvold, H. A. Eide, K. Stamnes, W. Li, J. Nieke, Y. Nakajima, F. Takahashi (2007). ADEOS-II/GLI snow/ice products — Part II: Validation results using GLI and MODIS data. *Remote Sensing of Environment*, 111, 274–290.

Bentley, W. A., Snow crystals (McGraw-Hill; 1st edition, 227 pp., 1931).

Bodhaine, B. A., N. B. Wood, E. G. Dutton, J. R. Slusser (1999). On Rayleigh Optical Depth Calculations. *J. Atmos. Oceanic Technology* **16**, 1854-1861.

Brun, E., Martin, E., Simon, V., Gendre, C., and Coleou, C. Salisbury, J. W., D'Aria, D. M., and Wald, A. (1994): An energy and mass model of snow cover suitable ments of thermal infrared spectral reflectance of frost, snow, for operational avalanche forecasting. *J. Glaciol*. 35:333–342.

Brun, E., David, P., Sudul, M., and Brugnot, G. (1992), A nu- Sergent, C., Pougatch, E., Sudul, M., and Bourdelles, B. Numerical model to simulate snow-cover stratigraphy for operational avalanche forecasting. *J. Glaciol*. 38:13–22.

Domine, F., M. Albert, T. Huthwelker, H.-W. Jacobi, A. A. Kokhanovsky, M. Lehning, G. Picard, and W. R. Simpson (2008). Snow physics as relevant to snow photochemistry. *Atmos. Chem. Phys*., 8, 171-208.

Frank, F. C., (1974). Descartes' Observations on the Amsterdam Snowfalls of 4, 5, 6 and 9 February 1634. *J. Glaciology* **13**, 535.

Green, R. O., J. Dozier, D. A. Roberts, & T. H. Painter (2002). Spectral snow reflectance models for grain size and liquid water fraction in melting snow for the solar reflected spectrum. *Annals of Glaciology*, 34, 71-73.

Grenfell, T. C.,Warren, S. G., &Mullen, P. C. (1994). Reflection of solar radiation by the Antarctic snow surface at ultraviolet, visible, and near-infrared wavelengths. *J. Geophys. Res.*, 99(D9), 18669−18684.

Hooke, R., Micrographia (Courier Dover Publications, 384 pp, 2003). ISBN:0486495647.

Hori M, T. Aoki, K. Stamnes, W. Li (2007). ADEOS-II/GLI snow/ice products — Part III: Retrieved results. *Remote Sensing of Environment,* 111, 291–336.

Hudson, S. R., S. G. Warren (2007). An explanation for the effect of clouds over snow on the top-of-atmosphere bidirectional reflectance. *J. Geophys. Res.*, 111(D18), doi:10.1029/2007/JD008541.

Hudson, S. R., S. G. Warren, R. E. Brandt, T. C. Grenfell, D. Six (2006). Spectral bidirectional reflectance of Antarctic snow: Measurements and parameterization. *J. Geophys. Res.*, 112(D19202), doi:10.1029/2006/JD007290.

Kepler, Johannes, 1611. *The Six-Cornered Snowflake*, translated by L. L. Whyte, 1966 (Oxford Univ. Press)

Kneizys, F. X., L. W. Abreu, G. P. Anderson, J. H. Chetwynd, E. P. Shettle, A. Berk, L. S. Bernstein, D. C. Robertson, P. Acharya, L. S. Rothman, J. E. A. Selby, W. O. Gallery, S. A. Clough, 1996: The MODTRAN 2/3 Report and LOWTRAN 7 Model. MODTRAN Report: Ontar Corporation, North Andover, MA, 261 pp.

Kokhanovsky A., and Zege, E. P. (2004), Scattering optics of snow. *Applied Optics*, 43, 1589–1602.

Kokhanovsky, A. A., T. Aoki, A. Hachikubo, M. Hori, E. P. Zege (2005). Reflective properties of natural snow: approximate asymptotic theory versus in situ measurements. *IEEE Trans. Geosci. Rem. Sens.*, 43, 1529-1535.

Kokhanovsky, A. A. (2006). Cloud Optics. Berlin: Springer.

Kokhanovsky, A. A. (2006). Scaling constant and its determination from simultaneous measurements of light reflection and methane adsorption by snow samples, *Opt. Letters*, 31, 3282-3284.

Li, W., K. Stamnes, B. Chen, X. Xiong (2001). Retrieval of the depth dependence of snow grain size from near-infrared radiances at multiple wavelengths. *Geophys. Res. Letters*, 28, 1699-1702.

Lyapustin, A. I., Atmospheric and geometrical effects on land surface albedo (1999). *J. Geophys. Res.*, **104**, 4123-4143.

Lyapustin, A. (2003). Interpolation and Profile Correction (IPC) method for shortwave radiative transfer in spectral intervals of gaseous absorption. *J. Atmos. Sci.*, **60**, 865-871.

Lyapustin, A. (2005). Radiative Transfer Code SHARM for Atmospheric and Terrestrial Applications, *Appl. Optics*, **44**, 7764-7772.

Lyapustin, A., and Y. Wang (2007). MAIAC: Multi-Angle implementation of atmospheric correction for MODIS. Algorithm Theoretical Basis Document, 69 pp., available at http://neptune.gsfc.nasa.gov/bsb/subpages/index.php?section=Projects&content=MAIAC%20ATDB.

Mie, G. (1908), Bitrage zur Optik truber Medien speziell kolloidaler Metallosungen, *Annalen der Physik*, 25, 377-445.

Mishchenko, M. I., J. M. Dlugach, E. G. Yanovitskij, and N. T. Zakharova (1999). Bidirectional reflectance of flat, optically thick particulate layers: An efficient radiative transfer solution and applications to snow and soil surfaces. *J. Quant. Spectrosc. Radiat. Transfer*, **63**, 409-432.

Mlawer, E. J., D. C. Tobin, and S. A. Clough (2006) A Revised Perspective on the Water Vapor Continuum: The MT_CKD Model, in preparation.

Nakaya, U., Snow Crystals: Natural and Artificial (Harvard University Press, 1954).

Nolin, A. W. and Dozier, J. (1993), Estimating snow grain size using AVIRIS data. *Remote Sensing of Environment*, 44, 231–238.

Painter, T. H., Dozier, J., Roberts, D. A., Davis, R.E. and Greene, R.O. (2003), Retrieval of subpixel snow-covered area and grain size from imaging spectrometer data. *Remote Sensing of Environment*, 85, 64–77.

Rothman, L. S., Barbe, A., Benner, D. C., Brown, L. R., Camy-Peyret, C., Carleer, M. R., Chance, K. V., Clerbaux, C., Dana, V., Devi, V. M., Fayt, A., Flaud, J.-M., Gamache, R. R., Goldman, A., Jacquemart, D., Jucks, K. W., Lafferty, W. J., Mandin, J.-Y., Massie, S. T., Nemtchinov, V., Newnham, D. A., Perrin, A., Rinsland, C. P., Schroeder, J., Smith, K. M., Smith, M. A. H., Tang, K., Toth, R. A., Vander, Auwera J., Varanasi, P., Yoshino, K. (2003). The HITRAN Molecular Spectroscopic Database: Edition of 2000 Including Updates through 2001. *J. Quant. Spectrosc. Radiat. Transfer*, *82*, 5-44.

Scambos, T. A., T. M. Haran, M. A. Fahnestock, T. H. Painter, J. Bohlander (2007). MODIS-based mosaic of Antarctica (MOA) data sets: Continent-wide surface morphology and snow grain size. *Remote Sensing of Environment,* 11, 242–257.

Stamnes, K., W. Li, H. Eide, T. Aoki, M. Hori, R. Storvold (2007). ADEOS-II/GLI snow/ice products – Part I: Scientific Basis. *Remote Sensing of Environment,* 111, 258–273.

Steffen, K., J. E. Box, and W. Abdalati (1996). Greenland Climate Network: GC-Net, in Colbeck, S. C. Ed. CRREL 96-27 Special Report on Glaciers, Ice Sheets and Volcanoes, trib. to M. Meier, pp. 98-103.

Tedesco, M. (2007a). Snowmelt detection over the Greenland ice sheet from SSM/I brightness temperature daily variations. *Geophys. Res. Lett*., 34, L02504,doi:10.1029/2006GL028466.

Tedesco, M. (2007b). A new record in 2007 for melting in Greenland. EOS, 88, No. 39, 25 Sept. 2007, p. 383.

Tedesco, M., and A. Kokhanovsky, (2007). The semi-analytical snow retrieval algorithm and its application to MODIS data. *Remote Sensing of Environment*, 111, 228 – 241.

Tedesco, M., W. Abdalati, and H. J. Zwally, (2007). Persistent surface snowmelt over Antarctica (1987–2006) from 19.35 GHz brightness temperatures, *Geophys. Res. Lett*., 34, L18504, doi:10.1029/2007GL031199.

Tomasi, C., et al., Aerosols in polar regions: A historical overview based on optical depth and in situ observations (2007). *J. Geophys. Res.*, 112, D16205, doi: 10.1029/2007JD008432.

Warren, S. G., R. E. Brandt (2008). Optical constants of ice from the ultraviolet to the microwave: A revised compilation. *J. Geophys. Res*. (in press).

Wiscombe, W. J., S. G. Warren (1980). A model for the specrtal albedo fo snow. I. Pure snow. *J. Atmos. Sci*., 37, 2712-2733.

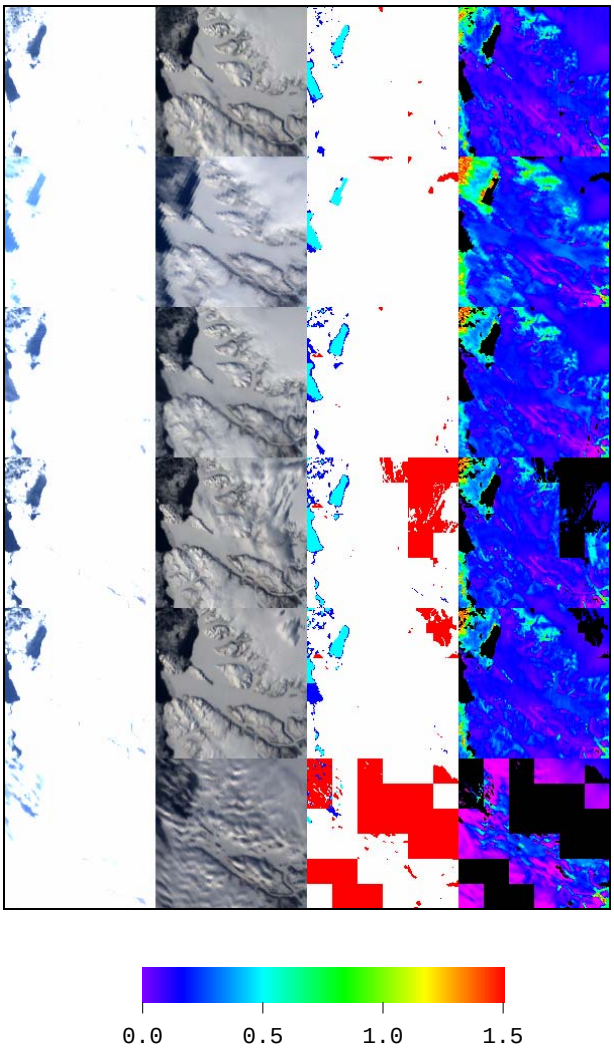

Figure 1. Illustration of *MAIAC* cloud mask for two consecutive days 112-113 of 2004 of MODIS TERRA observations over Thule, Greenland (the area of 150×150 km^2). The left two columns show the RGB image of gridded MODIS L1B data. They are normalized differently to help distinguish clouds over the snow. The third column shows *MAIAC* cloud mask, which uses the following legend: red – cloud; white, blue and light blue – clear over snow, land and water, respectively. The last column shows the retrieved snow grain size (see section 3).

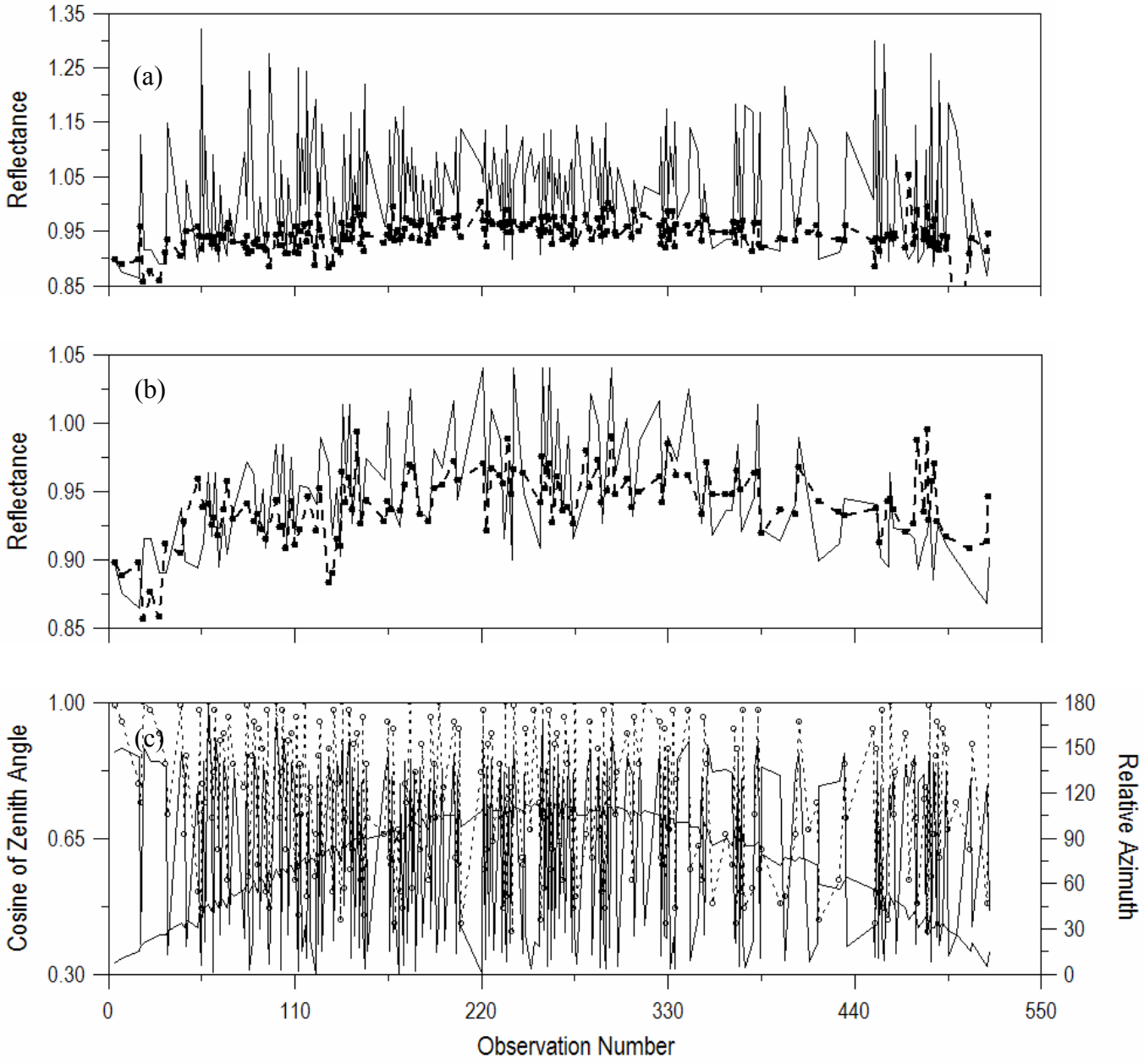

Figure 2. Comparison of function R_0 (solid line) with atmospherically corrected MODIS TERRA reflectance in the Blue band (0.47 μm) for the Saddle site. The top figure (a) shows the full set of clear-skies measurements. The bottom figure (b) shows the reduced dataset with forward scattering directions ($\varphi \leq 40^o$) filtered. The bottom plot (c) shows the geometry of observations for the full set of measurements. The smooth solid line and dashed line with circles show the cosine of solar and view zenith angles, respectively. The rapidly changing solid line shows the relative azimuth.

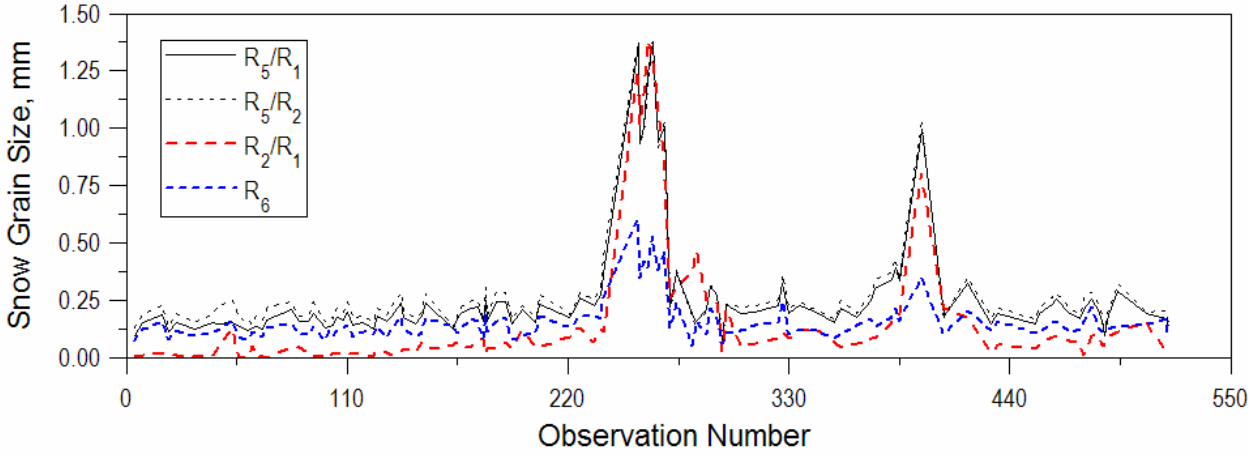

Figure 3. A time series of the derived snow grain size over Saddle, Greenland, for the period of March – September 2004. The retrievals used the following channels: B1 (0.645 μm), B2 (0.87 μm), B5 (1.24 μm), B6 (1.64 μm). The x-axis shows the number of MODIS TERRA consecutive observation.

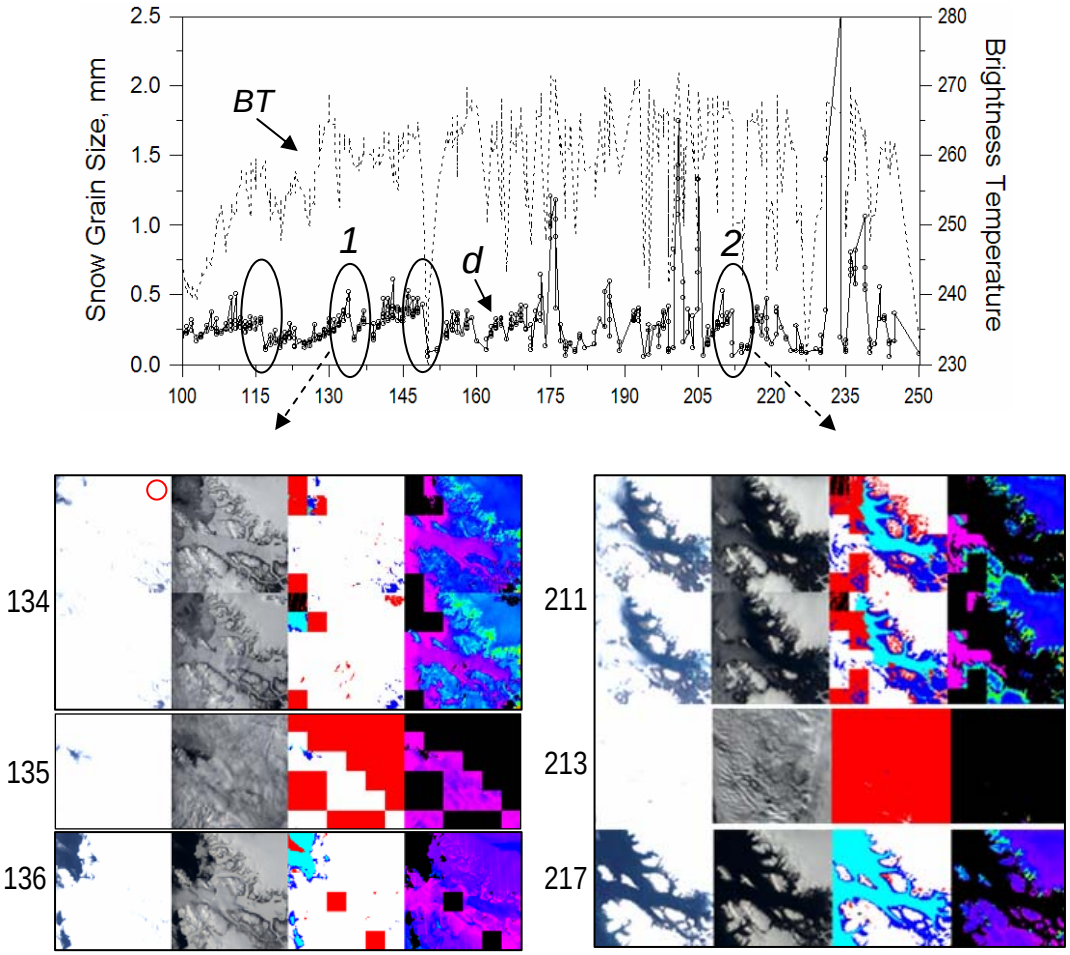

Figure 4. (Top) A time series of the snow grain size and brightness temperature for the area shown by a red circle near Thule, Greenland. (Bottom) MODIS TERRA RGB images, cloud mask, and retrieved snow grain size for the periods 1 (days 134-136) and 2 (days 211-217).

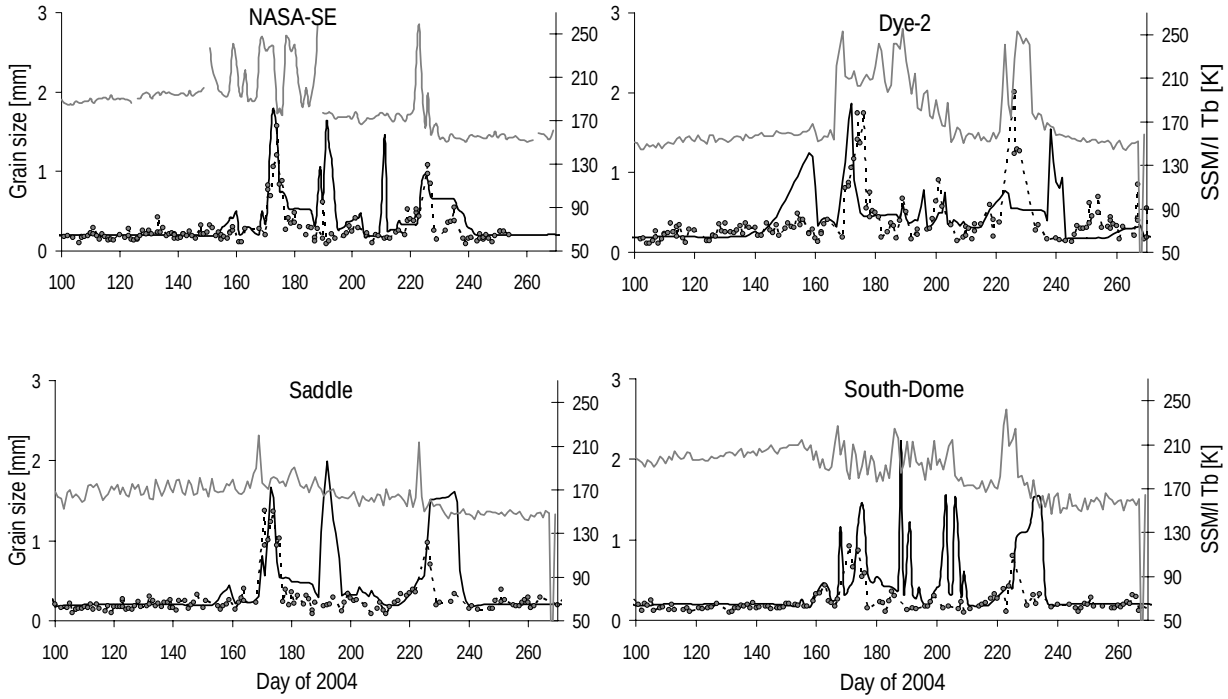

Figure 5. Comparison of the time series of snow grain size and SSM\I brightness temperature for four sites of Greenland. The gray line show SSM\I brightness temperature, the solid line shows CROCUS SGS reduced by a factor of two, and circles connected by a dashed line show MODIS-retrieved SGS.

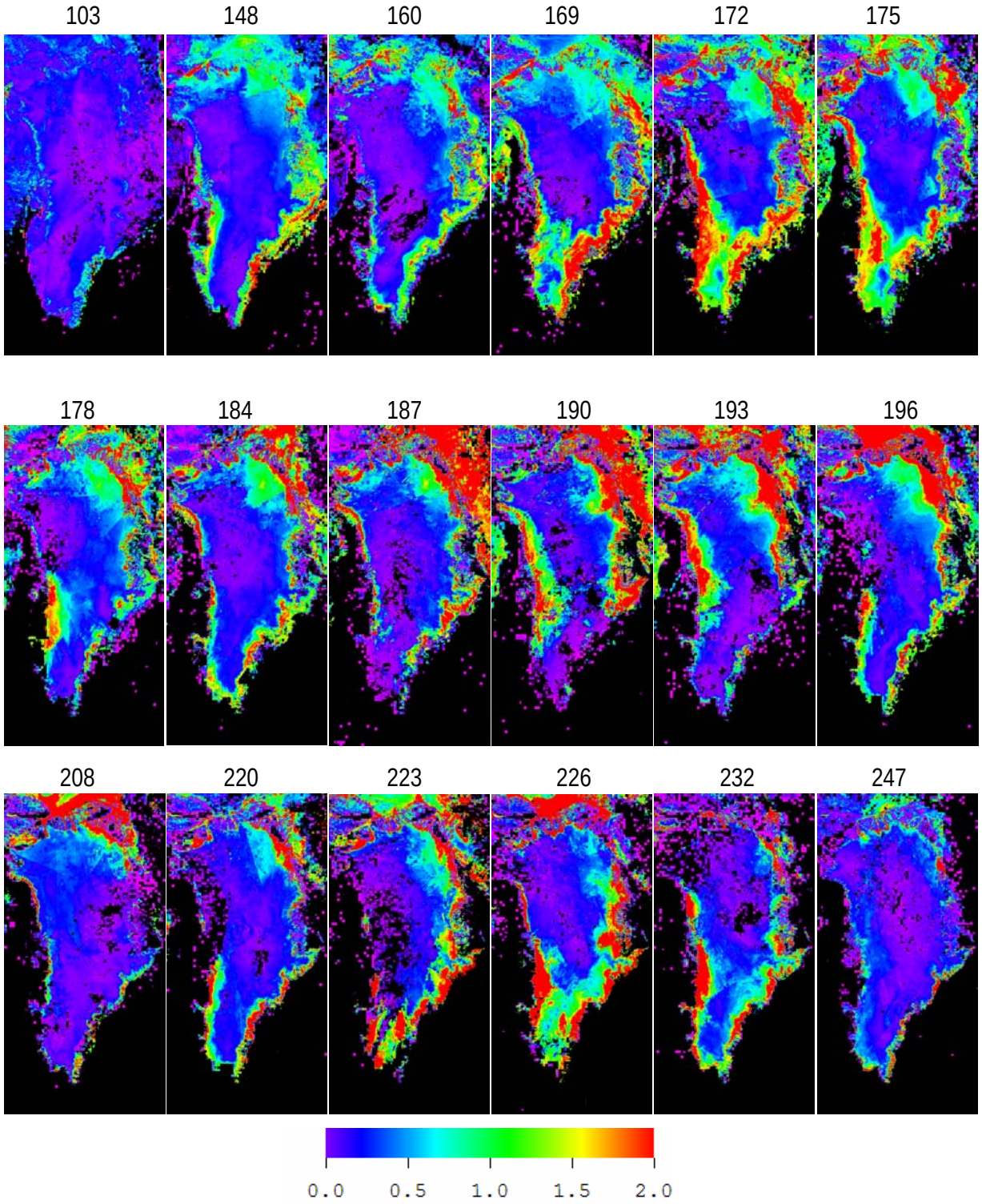

Figure 6. Snow grain size (mm) retrieved from MODIS TERRA data for the melting period of 2004 over Greenland. Each image is obtained as a 3-day composite to cover gaps caused by clouds.

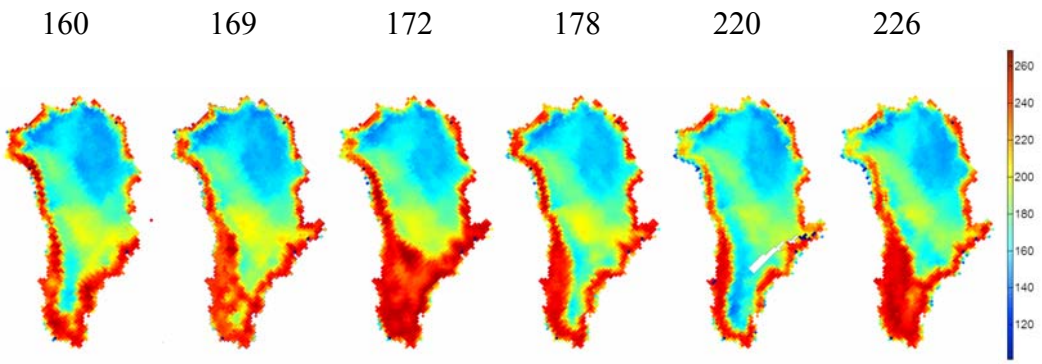

Figure 7. SSM\I brightness temperature over Greenland for 2004.